## Silicon Nanosheets as Candidates for Silicon-Based Optoelectronics

B. J. Ryan<sup>a</sup>, B. T. Diroll<sup>b</sup>, Y. Guo<sup>c</sup>, C. J. Dolgos<sup>a</sup>, Q. H. Wang<sup>c</sup>, L. T. Roling<sup>a</sup>, M. G. Panthani<sup>a</sup>

- <sup>a</sup> Department of Chemical and Biological Engineering, Iowa State University, Ames, Iowa 50011, United States of America
- <sup>b</sup> Center for Nanoscale Materials, Argonne National Laboratory, Lemont, Illinois 60439, United States of America
  - <sup>c</sup> Materials Science and Engineering, School for Engineering of Matter, Transport and Energy, Arizona State University, Tempe, Arizona 85287, United States of America

The growth in computational ability over the past decades has positively impacted global development, the economy, healthcare, and science. As on-chip components are approaching the atomic scale, alternative paradigms are needed to address the thermal and electronic issues that impose bottlenecks for computing. One approach to address this is with optoelectronics. However, silicon the backbone of microelectronics—is a poor choice due to its indirect bandgap, while existing optoelectronic materials are incompatible with CMOS infrastructure. Monolayer silicon nanosheets (SiNSs) are an intriguing material that exhibit photoluminescence, and are compositionally-compatible with the CMOS process. Here, we synthesize and characterize monolayer SiNSs, and show spectroscopic evidence that they exhibit a quasidirect bandgap, which is corroborated by DFT calculations. We probe their thermal stability, demonstrating their structure and photoluminescence are stable beyond the required operating temperatures for computing applications. These optoelectronic properties, CMOS-compatibility, and stability make SiNSs a viable candidate for silicon-based photonics.

### Introduction

Semiconductors are ubiquitous in electronic devices, found in applications such as photodetection (1), computing (2–4), energy conversion (5–8), and healthcare (9–11). At the core of nearly all of these electronic devices is silicon (Si), which has been the platform for computing technologies for the past five decades. Compared to other materials that could be used for computing, Si is earth-abundant, non-toxic, inexpensive, and forms an oxide that is chemically and electronically stable. Furthermore, the existing infrastructure that is dedicated to manufacturing, purifying, and distributing Si is tremendous, motivating the continued use of Si as the platform for computing in the future. In the past few decades, new technologies have emerged that utilize light, instead of electricity, to transmit information. However, integrating these technologies on Si-based computer chips has been challenging. Thus, researchers have sought routes to inducing light emission in Si (12–15).

Light emission in nanostructured Si is well-documented, (13,16–18) and two-dimensional (2D) materials have demonstrated extraordinary potential for electronic and optoelectronic applications. Thus, SiNSs are a potentially exciting material that could harness the unique properties of 2D materials while also being CMOS compatible. Indeed, SiNSs have recently gained much interest because of their direct-like bandgap behavior that results in efficient light emission (19,20). However, in order for these SiNSs to be considered practical candidates for Si-based photonics, the thermal stability under operating conditions must be evaluated. A common standard for commercial, industrial, and military applications is that devices remain operable up to temperatures of ~125 °C.

Here, we explore the properties of SiNSs that are relevant for next-generation optoelectronics. First, we characterize the structural and optical properties of SiNSs that were synthesized by the topotactic deintercalation of CaSi<sub>2</sub> in aqueous HCl at -35 °C. Then, we characterize the high- and low-temperature stability, structural properties, and optical properties of the SiNSs. Finally, we characterize the stability of the SiNSs against oxidation.

### **Results & Discussion**

SiNSs are synthesized by the topotactic deintercalation of CaSi<sub>2</sub> with HCl at ~-35 °C (Figure 1). CaSi<sub>2</sub> is a layered Zintl-phase structure consisting of a corrugated, anionic monolayer of Si atoms stabilized by Ca<sup>2+</sup> cations (19,21,22,23). The sheets of Si consist of

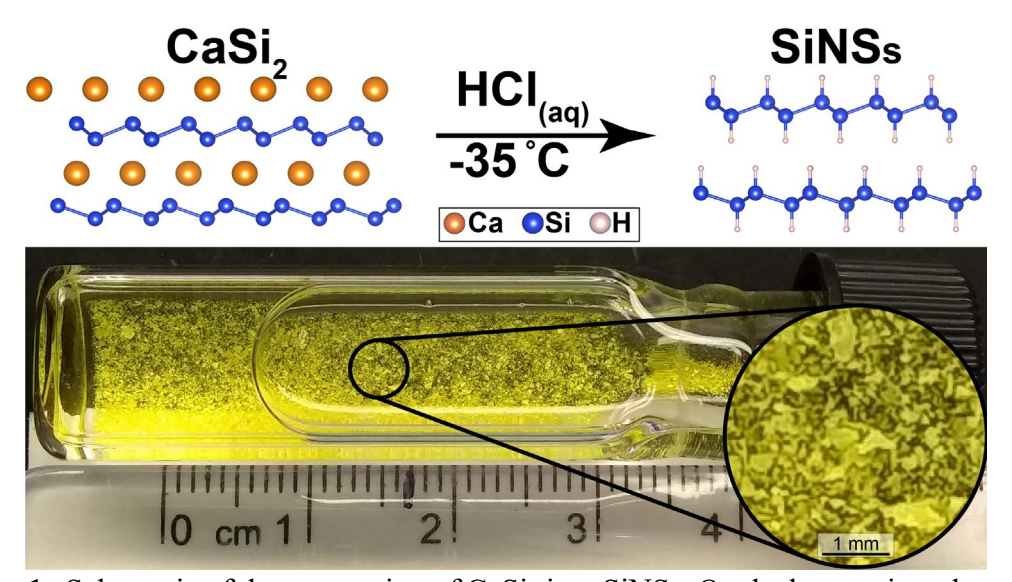


**Figure 1.** Schematic of the conversion of CaSi<sub>2</sub> into SiNSs. On the bottom is a photograph of the SiNSs in cuvette filled with methanol.

a monolayer of the Si (111) plane. Upon combining CaSi<sub>2</sub> with HCl, the Si sheet is protonated, yielding predominantly hydrogen-terminated SiNSs (though silicon oxides and chlorides are often present) and CaCl<sub>2</sub> as a byproduct. The CaCl<sub>2</sub> is then washed away to yield SiNSs.

To characterize the structure of the SiNSs, we collected total X-ray scattering using synchrotron radiation, and present the azimuthally-integrated total X-ray scattering (AI-TXS) in Figure 2a. The AI-TXS consists of broad features associated with the  $\{hk\ell\}$  (for

 $\ell > 0$ ) reflections, indicating that the SiNSs have a significant degree of disorder among the intersheet spacing, as the (006) plane corresponds to the intersheet spacing—with six nanosheets per nominal unit cell. However, the peaks corresponding to the  $\{hk0\}$  (for h and k > 0) reflections are much sharper than the other features, indicating that the translational registry among adjacent nanosheets is well-preserved during the deintercalation process.

We characterized the surface chemistry of the SiNSs using FTIR and Raman spectroscopy (Figure 2b–c). The FTIR spectrum consists of vibrations corresponding to SiH at 2092, 737, 633, and 507 cm<sup>-1</sup>; SiOH at 3600 and 900 cm<sup>-1</sup>; SiO at 1177 and 1019 cm<sup>-1</sup>; and SiCl at 571 cm<sup>-1</sup>. Additionally, there are residual traces of water within the sample, as indicated by the vibrational modes centered at ~1600 and ~3300 cm<sup>-1</sup>. It is important to note that the relative FTIR intensity of features does not accurately correspond to the concentration of a given component; we previously determined that SiO-containing vibrations are ~30 times greater in intensity than the SiH vibrations for the same concentration (19). The Raman spectrum consists of vibrational modes of SiH at 2132, 730, 640, 507 cm<sup>-1</sup>, which agrees well with FTIR; SiOH at ~930 cm<sup>-1</sup>; and 2D SiSi vibrations at 500 and 385 cm<sup>-1</sup>. These results are consistent with our previous report (19), and indicate that the SiNSs consist of a 2D Si framework that is primarily terminated with hydrogen, but silicon oxides and chlorides are also present in low concentrations.

We then sought to characterize the absorbance and photoluminescence (PL) emission properties of the SiNSs (Figure 2d–e). The absorbance of the sample was inferred by converting diffuse reflectance data into the well-known Kubelka-Munk (KM) function (24). The KM data demonstrates a sharp onset of absorbance at ~490 nm (2.53 eV). Intriguingly, the PL emission spectrum has its maximum at 508 nm (2.44 eV). Such similar values of the onset of absorption and maximum of emission are characteristic of direct band gap emission. This makes the SiNSs an attractive material for next-generation Si-based photonics.

The lifetime of the excited states was characterized with time-resolve photoluminescence (TRPL, Figure 2e). Note that in Figure 2e, both the intensity and the time are plotted on log-scale. We find a decrease in PL intensity of 99% of its initial value by 100 ns—despite the PL emission extending past 2  $\mu$ s. We find that the emission is characterized by a fast, intermediate, and long decay lifetime. We fit this emission decay to a triexponential decay (see methods for additional details), with decay times (coefficients) as follows:  $\tau_1 = 0.78$  ns ( $A_1 = 0.84$ ),  $\tau_2 = 13.8$  ns ( $A_2 = 0.14$ ), and  $\tau_3 = 365$  ns ( $A_3 = 0.02$ ). Thus, it is clear to see that the excited state decay is dominated by the very fast decay. At a low temperature (5 K, not shown), we find only a slight increase in the overall lifetime, with decay times (coefficients) as follows:  $\tau_1 = 1.15$  ns ( $A_1 = 0.82$ ),  $\tau_2 = 20.4$  ns ( $A_2 = 0.15$ ), and  $\tau_3 = 478$  ns ( $A_3 = 0.03$ ).

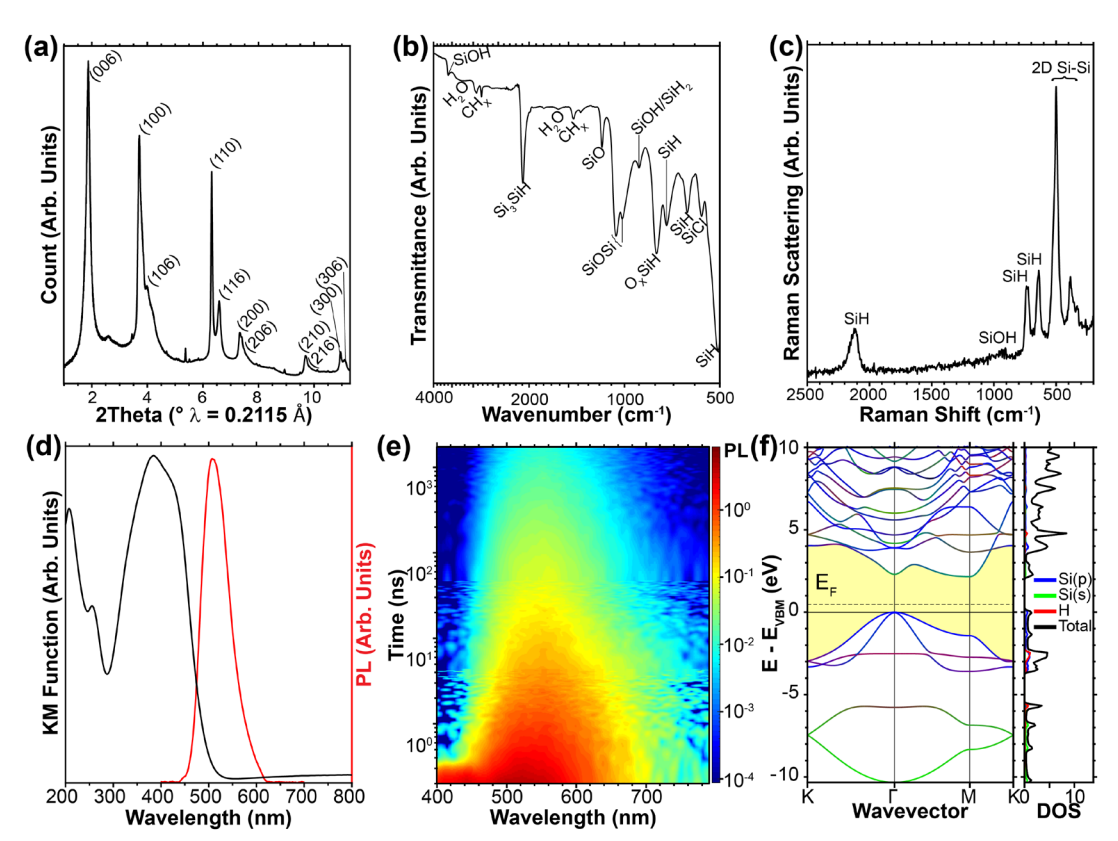


**Figure 2.** (a) Azimuthally-integrated total X-ray scattering data of the SiNSs. (b) FTIR and (c) Raman of the SiNSs. (d) Kubelka-Munk (left, black axis) and steady-state PL (right, red axis) of SiNSs. (e) TRPL of a film of SiNSs collected at 300 K. Note that both the intensity (color) and time (y-axis) are both on log-scale. The horizontal lines in the data at ~4 and ~40 ns are a result of splicing together three sets of data. (f) DFT simulations of the band structure of a single hydrogen terminated SiNSs; the horizontal dashed line corresponds to the Fermi level (E<sub>F</sub>). Note that the color of the bands corresponds to pDOS to enable visualization of the orbital contribution to specific bands.

To rationalize the relatively intense PL and short carrier lifetime from the SiNSs, we calculated the band structure of a single hydrogen-terminated SiNS (Figure 2f). The band structure indicates a nearly-direct bandgap, with the direct transition being only ~0.1 eV greater in energy than the indirect transition. It is important to note that the confined dimensionality of the SiNSs causes the momentum conservation to be relaxed due to Heisenberg uncertainty (25). Thus, it can be rationalized that some of the emission from the SiNSs emerges from a direct transition. To characterize thermal stability, we annealed SiNSs over a range of temperatures under an inert atmosphere. We collected total X-ray scattering, FTIR, diffuse reflectance, TGA, DSC, and FTIR of the volatile gaseous decomposition products that evolved during the TGA/DSC measurement (Figure 3). Between 25–300 °C, there is no detectible change in the AI-TXS pattern. However, beginning at ~350 °C, there is a sudden broadening of all reflections, which we attribute to amorphization of the Si framework. At an annealing temperatures of 425 °C or greater, the AI-TXS data resembles that of amorphous Si.

We collected FTIR spectra to probe changes in the surface chemistry as the SiNSs are annealed (Figure 3b). Similar to the AI-TXS data, we observe no discernable change in the FTIR spectra between 25-300 °C, except for the decrease in the H<sub>2</sub>O signal at ~1600 and

3400 cm<sup>-1</sup>; this loss of water is corroborated by the endothermic peak in the DSC data (Figure 3d, left axis), the mass loss in TGA (Figure 3d, right axis), and the presence of water vapor in the exhaust gas (Figure 3e) at ~100 °C. However, by 350 °C, there is a stark decrease in the SiH signals at 2132, 730, 640, and 507 cm<sup>-1</sup>. This suggests that the onset of amorphization of the Si framework is accompanied by the loss of H. We also note that this loss of H occurs in tandem with a sudden increase in electron paramagnetic resonance (EPR) intensity (not shown), indicating the formation of radicals. Thus, we attribute the amorphization of the Si framework to the formation of Si dangling bonds as hydrogen is liberated from the Si surface. This trend of decreasing SiH signal continues to 425 °C, but importantly, the SiH signal is not completely gone; this signal of SiH bonds within amorphous Si is typical (26–28). At ~350 °C, the SiCl signal at 571 cm<sup>-1</sup> dramatically decreases and is corroborated by the FTIR signal in the exhaust gas during decomposition, where HCl vapor is detected beginning at ~350 °C (Figure 3e).

Lastly, to assess changes in optical properties of the SiNSs, we used KM transformation of the diffuse reflectance and PL of SiNSs at different annealing temperatures (Figure 3c and f). Again, similar to the aforementioned AI-TXS and FTIR data, there is little change in the KM data between 25–300 °C. However, by 350 °C, the onset of absorption begins to red shift, and continues to do so up to 425 °C where the onset is ~750 nm (1.65 eV) and is consistent with amorphous Si (29). The PL signal (Figure 3c) undergoes little change up to 100 °C, but by 200 °C, there is a decrease in the PL intensity. Between 200 and 300 °C is the largest differential decrease in the PL intensity, and by ~400 °C the PL signal is nearly undetectable. It is interesting to note that the PL signal undergoes changes at temperatures below where the AI-TXS, FTIR, and the KM data begin to change. We suspect that small quantities of H are liberated from the Si-H surface at these relatively-low temperatures, leading to a small concentration of non-radiative dangling bonds.

In the following, we summarize the high-temperature properties of the SiNSs. The Si framework is remarkably stable up to ~350 °C, after which it undergoes structural amorphization. This amorphization is accompanied by the loss of terminal functional groups that give rise to Si dangling bonds. By ~425 °C, the structure of the Si framework and the optical properties resemble that of amorphous Si. The PL emission, however, appears to undergo changes at temperatures below 350 °C, with a decrease in PL intensity beginning by 200 °C. However, the PL signal is still detectable by ~350 °C. These results indicate that these SiNSs can be used in commercially-available devices, as these SiNSs retain most of their original properties at the upper limit of operating temperatures (125 °C). These results suggest that by functionalizing the SiNSs with ligands that form more thermally stable bonds (such as carbon chains that form Si-C bonds), the optical properties could be retained up to even higher temperatures.

To obtain a better understanding of the optical properties, we conducted low-temperature PL and TRPL measurements of films of SiNSs (Figure 4). Due to the inability to make uniform homogeneous films, we were unable to collect quantitative temperature-dependent intensity data, but we note that the PL intensity does generally increases as temperature decreases. To obtain a deeper understanding of the PL data we sought to fit the PL to a Gaussian distribution, but the asymmetry of the PL necessitated fitting the data to two Gaussian distributions to obtain reasonable fits. The PL, FWHM, percent contribution, and peak positions are shown in Figure 4a–d. We find that the FWHM of both Gaussian distributions change at very similar rates throughout the entire temperature range.

The FWHM of both Gaussian distributions decreases from 300 K to 100 K. At temperatures below 100 K, the FWHM increases slightly down to 5 K. We attribute this decrease and then increase of the FWHM to be related to freezing out trap states and potentially a decrease in transitions from the M-point and increased cooling to radiative states, as discussed below. Overall, we find that the percent contribution of each distribution varies only slightly over the entire temperature range, with the low energy feature decreasing from 46% to 43% from 300 to 5 K.

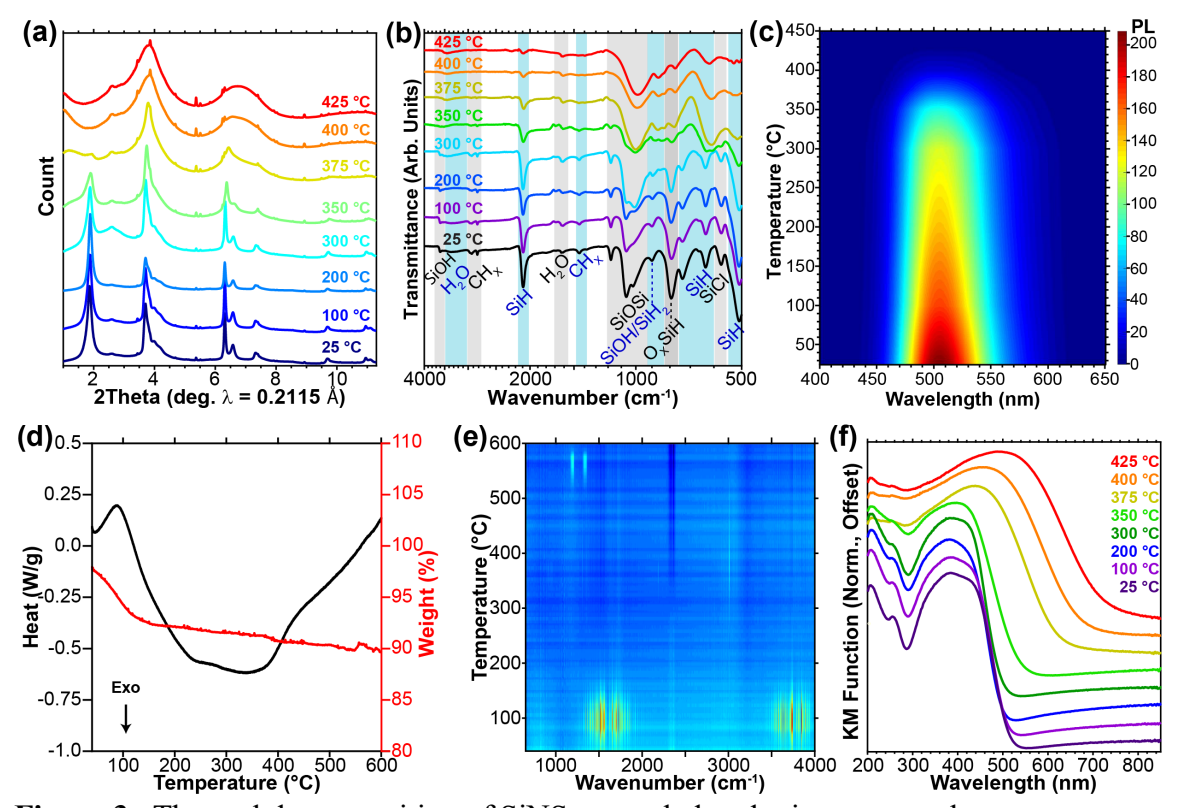


**Figure 3.** Thermal decomposition of SiNSs annealed under inert atmosphere. (a) Azimuthally-integrated total X-ray scattering and (b) FTIR of SiNSs that have been annealed at various temperatures; vertically-oriented blue and grey regions are to guide the eye. (c) PL of SiNSs annealed at various temperatures. All samples were collected at a concentration of 0.5 mg/mL. (d) Thermal gravimetric analysis (black, left axis), and differential scanning calorimetry (right, blue axis). (e) FTIR of the gaseous decomposition products from the TGA/DSC data. (f) Kubelka-Munk (KM) function of SiNSs that have been annealed under inert atmosphere.

The PL peak position of the experimental data and the peak position of the two distributions are shown in Figure 4d. We then fit all three of these peak locations to the widely utilized Varshni fit (Equation 1) (30):

$$E_{G}(T) = E_{G0} - \alpha \frac{T^{2}}{\beta + T} \tag{1}$$

where  $E_{G0}$  is the bandgap at 0 K, and  $\alpha$  and  $\beta$  are fitting parameters. Despite  $\alpha$  and  $\beta$  being purely empirical, it has been suggested that  $\beta$  is related to the Debye temperature (30). However, to the best of our knowledge, there are no reports that attempt to determine the Debye temperature of SiNSs. We do note that the value of  $\beta$  does generally align well with a maximum in the lifetime of temperature-dependent PL (*vide infra*). Given that the SiNSs have intense SiH FTIR modes that occur at frequencies much higher than any frequency

found in bulk Si, we suspect that the Debye temperature of SiNSs to be greater than that of Si (645 K). The values of the fitting parameters are shown in Table 1.

**TABLE I.** Fitting parameters to the Varshni equation.

Peak	E <sub>G0</sub> (eV)	α (10 <sup>-4</sup> eV/K)	β (K)
Overall	2.25	5.10	154.7
High Energy	2.27	3.35	117.4
Low Energy	2.08	3.62	219.6

To assess whether structural phase transitions occur, we collected temperature dependent total-scattering synchrotron XRD data and present the AI-TXS data in Figure 4g down to the temperature limits of the instrument (100 K). We find no appreciable structural changes within this temperature range, with only a contraction of the c-axis of 0.07 Å, which is considered negligible as the step size of the instrument is only 0.035 Å. Since there are no structural changes down to 100 K, we attribute the changes in the PL to temperature-induced changes in the excitonic landscape. However, we cannot conclusively rule out structural changes below 100 K.

The TRPL indicates that the exciton lifetime is not a single exponential (Figure 4e). Further, we tried fitting the TRPL data to a biexponential decay, but it too gave insufficient fits. As such, we fit the data to a triexponential decay and it gave good fits. Multiexponential decays are very typical for Si nanomaterials (31). We also fit the TRPL data to a stretched exponential decay. The stretched exponential decay has also been used to model TRPL data for many Si nanomaterials (32). The downside to the stretched exponential decay is that it is not derived from first principles and does not have a precise direct physical interpretation. That said, the stretched exponential is generally used to model a distribution of relaxation times as a result of dispersive diffusion of excitons to recombination centers (33).

After fitting the TRPL data to both the triexponential decay and the stretched exponential decay, a characteristic average lifetime of each model was determined. The characteristic lifetimes are shown in Figure 4f. Both lifetimes yield similar results with the stretched exponential decays spanning a slightly larger range of decay times. Interestingly, both lifetimes give rise to a maximum lifetime around 100–150 K. In general, the triexponential decay does fit the data better than the stretched exponential decay, producing a goodness-of-fit (as determined by the sum of squared residuals, SSR) that is ~2 times better than the stretched exponential. However, if we account for the number of free variables within each fitting equation by multiplying the SSR by the number of free variables within each equation, the stretched exponential yields a better fit (the stretched exponential has three fitting parameters).

Another important factor in determining the viability of a material for optoelectronic applications is its stability against oxidation. As such, we exposed SiNSs to ambient air and assessed their vibrational and PL emission properties (Figure 5a–b). Upon comparing the FTIR spectrum of the air-exposed sample to the sample that was not exposed to ambient environment, we observe a few major changes. Most noticeably, there is an increase in the signal associated with water. Further, there is a stark change in the SiOSi vibrations centered at ~1020 cm<sup>-1</sup> with the overall signal intensity increasing and the doublet merging to yield a single, large broad feature as air-exposure is increased. This suggests that the

initially relatively-distinct SiOSi vibrational modes become more similar in nature as oxidation is increased, and is consistent with the formation of regions of amorphous SiO<sub>x</sub>. Additionally, the small, sharp SiO feature at  $\sim 1080~\rm cm^{-1}$  nearly disappears, but the broadening of the SiOSi region at  $\sim 1020~\rm cm^{-1}$  makes precise interpretation of this region difficult. There is also a sudden decrease in the CH<sub>x</sub> vibrations at  $\sim 2900~\rm and \sim 1450~\rm cm^{-1}$ , suggesting that any residual methanol from the washing procedure is liberated.

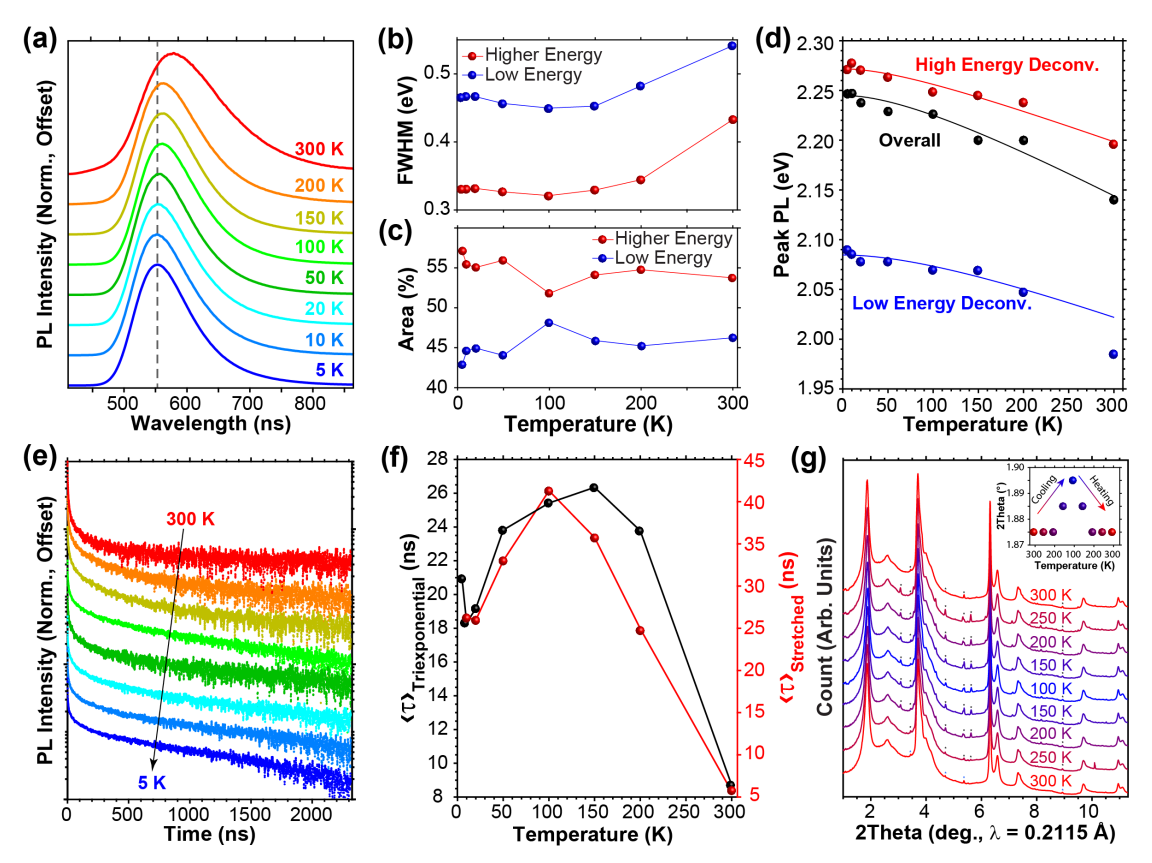


**Figure 4.** Low temperature PL measurements and fits of unannealed SiNSs. (a) PL of a film of SiNSs; vertical dashed line is to guide the eye. (b) and (c) are the results of the two-peak fit of the data shown in panel (a). (d) Varshni fits for the temperature-dependent PL. (e) TRPL and (f) average lifetime for the triexponential fit (left, black axis), and the stretched exponential decay (red, right axis) of a film of SiNSs. (g) Azimuthally-integrated total X-ray scattering of SiNSs cooled to 100 K and subsequently heated to 300 K; inset is the location of the peak centered at  $\sim$ 2 ° as a function of temperature. The small asterisks indicate a TaSi<sub>2</sub> impurity.

The SiH features at ~2100 and 504 cm<sup>-1</sup> decrease only slightly throughout the duration of oxygen exposure, but remain relatively unchanged. Overall, the largest differential change occurs after two days, with only slight changes thereafter. This plateau could be a result of the consumption of the oxygen within the vial within the first two days (see methods for experimental details). Interestingly, the SiH feature at ~740 cm<sup>-1</sup> nearly completely disappears after two days; the exact origin of this is uncertain, but we speculate that these SiH vibrations could be related to Si-H bonds near Si-O bonds. As such, as oxidation increases and the SiO structure changes, this could influence these Si-H bonds. Indeed, we performed DFT calculations on SiNSs containing oxygen, and find that it is enthalpically advantageous to form SiO bonds to Si atoms that are already oxidized (i.e.,

is more favorable to add an O to  $(O_XSi_{3-X})Si$ -H than it is for  $Si_3Si$ -H), as shown in Figure 5c. We calculated three different configurations for each number of oxygens contained within a SiNS, and are showing only the most energetically favorable configurations in Figure 5c and f. The fact that  $E_{Si_{32}H_{32}O} > E_{Si_{32}H_{32}O_2} > E_{Si_{32}H_{32}O_3}$  demonstrates that it is enthalpically favorable for a Si atom that is already oxidized to form additional bonds with oxygen compared to a non-oxidized Si atom. Thus, we conclude that as oxidation is increased, we would expect that the Si-H bonds near Si-O bonds to change, which is consistent with the experimental observation.

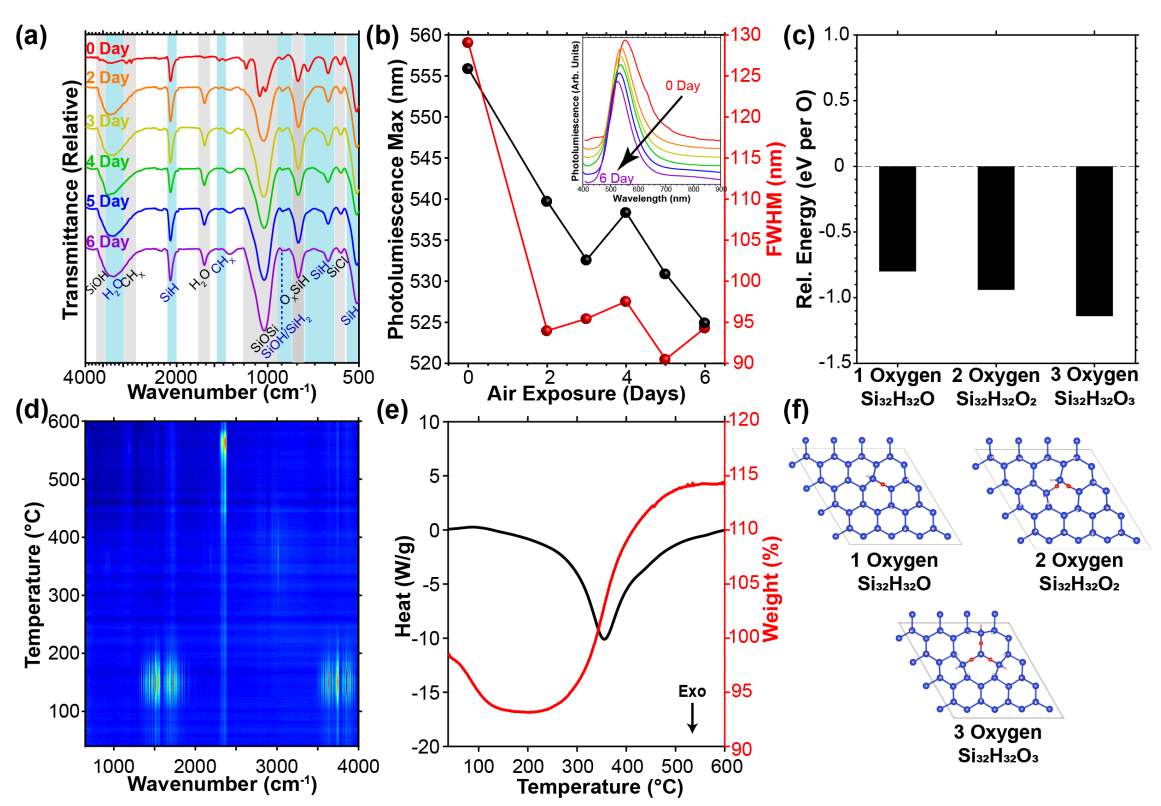


**Figure 5.** Stability of SiNSs upon exposure to ambient air. (a) FTIR of SiNSs that have been oxidized by exposure to air; the number of days on the figure indicates the number of days the sample was exposed to air. (b) Steady-state PL data with the peak location (black, left axis) and FWHM (red, right axis); the PL data is shown in the inset. (c) Energies of the oxygen-containing structures in panel (f). (d) The gaseous decomposition products as a function of annealing temperature; SiNSs were annealed in air. (e) Thermal gravimetric analysis (black, left axis), and differential scanning calorimetry (red, right axis). (f) Structures associated with the energies shown in panel (c).

We now turn our attention to the PL (Figure 5b). As exposure to air is increased, we see that the peak blue shifts by ~60 meV within the first two days of air exposure. This suggests that some of the radiative recombination sites are related to silicon oxides within the nanosheets, or to the structural distortions in the Si framework that emerge as oxidation occurs. Further, we see that the FWHM of the PL spectrum decreases as oxidation is increased.

Lastly, we characterized the thermal decomposition of the SiNSs upon heating in air with TGA and DSC; the volatile decomposition products were sent through an FTIR instrument for analysis (Figure 5d–e). The first notable feature is the loss of water between

~100–200 °C, as is made apparent by the water signals in FTIR accompanied by an endothermic peak in the DSC and a mass loss in TGA. As the sample is heated, the next feature occurs between ca. 300–425 °C where HCl vapor is detected in FTIR and is accompanied by a large exothermic peak in DSC and a sudden increase in mass; the increase in mass and large exothermic feature is attributed to the oxidation of the Si framework.

#### Conclusion

Our results demonstrate potential for integrating SiNSs into photonic devices. We found that the SiNSs are predominantly terminated with hydrogen atoms, with the presence of relatively low amounts of oxidation and chlorine termination. The proposed structure elucidated by these results is also consistent with DFT simulations. The onset of absorbance and peak location of photoluminescence emission are close in energy (showing a Stokes shift of ~0.09 eV), a property characteristic of direct-gap emission. Further analysis of emission through time-resolved data showed that the recombination primarily occurs on nanosecond time scales and can be fit to a triexponential decay, elucidating the emission kinetics and giving insight to potential device lifetimes.

Practical aspects of device dependability were also studied. As silicon is prone to oxidation, the SiNSs were tested over a range of air exposure times; with increased exposure, a blue shift in the photoluminescence occurred. Finally, both structural and optical property changes were monitored as a function of thermal annealing, determining degradation limits. Structurally, the SiNSs remained compositionally stable up to ~350 °C, after which hydrogen and chlorine are liberated from the nanosheets, accompanied by the amorphization of the silicon framework. The photoluminescence properties proved to be more susceptible to degradation, showing a noticeable decrease in intensity in temperatures around 200 °C, however still far exceeding industrial process needs. Overall, the results presented here show that SiNSs have promising optoelectronic properties and stability, providing a potential foundation for next-generation computing based on integrated photonic circuits.

#### Methods

### Experimental Methods:

<u>Chemicals:</u> Calcium (Sigma Aldrich, 99.95%), silicon (Sigma Aldrich, 99%), aqueous hydrochloric acid (Fisher, 36%, ACS plus), tantalum tube (the tube was cut to 3.25" long, with 0.500" OD and 0.020" wall thickness), and methanol (ACS grade were all purchased without additional purification.

<u>CaSi2</u>: All steps were performed in a glovebox filled with Ar unless otherwise specified. CaSi2 was synthesized by combining elemental sources of Si and Ca in a molar ratio of Si:Ca  $\approx 1:2.125$  in a tantalum (Ta) tube. The Ta tube was then welded shut. Warning! The Ta tube must be long enough to avoid over pressurization of the tube! Over pressurization can cause tube failure and a sudden release of molten material! This reaction shall be performed inside of an inert atmosphere, such as a glovebox! Then, the tube containing Ca and Si was placed into the coil of an induction heater. The tube was then heated until the

contents were molten; the contents were kept molten for ~1 minute before removing the tube from the coil, immediately inverting the tube, and the tube was allowed to cool until the contents solidified (~1 minute). This melting-inverting-cooling step was repeated for a total of four times. Then, the contents were melted once more and immediately removed from the coil and immediately placed in a container filled with aluminum chips to quickly cool the contents. The tube was removed from the glovebox and rinsed with concentrated hydrochloric acid to remove any aluminum that adhered to the tube. The tube was then dried, loaded back into the glovebox, and the CaSi<sub>2</sub> product was removed from the tube. A typical reaction yielded 5 g of CaSi<sub>2</sub>.

SiNSs: In a typical reaction, the SiNSs were synthesized by combining 2 g of CaSi<sub>2</sub> and 200 mL of HCl were pre-chilled to -35 °C. Under flowing N<sub>2</sub>, the CaSi<sub>2</sub> and HCl were combined in a round-bottom, three-necked flask; the flask is connected to a Schlenk line and is contained within a freezer set to -35 °C. The contents were allowed to react, unstirred, for 11 days under a blanket of constant N<sub>2</sub> flow. After 11 days, the product was then vacuum filtered on a Schlenk line under N<sub>2</sub> flow before loading the product into a glovebox filled with N<sub>2</sub>. Then, the product was washed with ~200 mL of anhydrous methanol to remove the CaCl<sub>2</sub> byproduct. The retentate (SiNSs) was then dried under vacuum for a few hours to yield the yellow SiNSs.

Annealed SiNSs: All procedures were performed in a glovebox filled with N<sub>2</sub>. The SiNSs were annealed by placing ~50 mg of the SiNSs into a glass vial. Then, an aluminum reaction block on a hot plate was heated to the desired temperature; the temperature was determined by measuring the temperature of the aluminum block with an external thermocouple. Once the desired temperature of the reaction block was achieved, the glass vial containing the SiNSs was placed inside of the reaction block for 5 minutes followed by briefly shaking the SiNSs, and were placed back in the reaction block and annealed for an additional 5 minutes. After this, the vial was removed from the reaction block and allowed to cool naturally inside the glovebox.

<u>Air-Exposed SiNSs:</u> Air-exposed SiNSs were prepared by taking SiNSs and placing them in a glass vial in a glovebox filled with N<sub>2</sub>. Then, the vial was removed from the glovebox, and in a fume hood, the cap was opened and the SiNSs were exposed to air for 10 minutes. The vial was then capped and left for the prescribed time (2, 3, 4, 5, and 6 days) before loading the SiNSs back into a glovebox filled with N<sub>2</sub>.

AI-TXS: Azimuthally-integrated total X-ray scattering data were collected at the Advanced Photon Source at Argonne National Laboratory and beamline 11-ID-B. An X-ray energy of 86720 eV and a 2D detector at a distance of 180 mm were used. The total X-ray scattering data were azimuthally integrated with the GSAS-II software (34) after calibrating to a CeO<sub>2</sub> standard.

<u>FTIR</u>: FTIR data were collected under ambient conditions with a Nicolet iS5 FTIR spectrometer with an iD5 Attenuated Total Reflectance (ATR) accessory.

Raman: Raman spectroscopy was conducted by the WITec alpha 300R confocal Raman microscope system. The laser excitation wavelength used during the characterization was 532 nm, and the objective lens used was 100X with  $\sim 1$   $\mu$ m diameter laser spot size. 0.3 mW laser power was used to minimize potential damage to the SiNSs sample.

Diffuse reflectance: Diffuse reflectance data were collected with a Perkin Elmer Lambda 750 equipped with a Labsphere integrating sphere (100 mm). The SiNS were dispensed onto the adhesive side of transparent, colorless packaging tape (3M Scotch® Packaging Tape), and reflectance were collected of the exposed SiNSs. The reflectance data was then transformed into the Kubelka-Munk (KM) function (24).

Steady-state photoluminescence: Steady-state PL data were collected with a Perkin Elmer LS 55 with an excitation wavelength of 370 nm. All samples kept air-free and were dispersed in anhydrous methanol for measurements.

TGA/DSC/FTIR: TGA, DSC, and FTIR heatmaps were collected by heating samples in an alumina (Al<sub>2</sub>O<sub>3</sub>) crucible under a flow of either N<sub>2</sub> or synthetic air (20 mol% O<sub>2</sub>, 80 mol% N<sub>2</sub>) at a flowrate of 10 mL/min. The exhaust gas of the TGA/DSC were sent through an FTIR instrument. The TGA/DSC was a Netzsch Jupiter STA449 F1, and the FTIR was a Bruker Tensor 37.

<u>Time-resolved photoluminescence</u>: Time-resolved photoluminescence was collected in two ways. For single wavelength measurements, a pulsed 405 nm laser diode (PicoQuant) was used to excite the sample. Emission was collected using an optical fiber and directed through a spectrometer to an avalanche photodiode for time-correlated single photon counting. The fluence of these measurements was <1 nJ/cm<sup>2</sup>. For broadband measurements of photoluminescence decay, a 2kHz amplified Ti: sapphire laser (SpectraPhysics) was frequency doubled to produce 400 nm pulses to excite the sample. Emitted photons were collected using an optical fiber and directed through a spectrometer on to a streak camera. The fluence of these measurements was  $\sim 2 \mu J/cm^2$ . Samples were measured as powders in an evacuated cryostat. The same configurations were used to collected time-integrated photoluminescence as a function of temperature by directing the emitted light through a spectrometer to a CCD array.

Data were fit to the following triexponential decay  $(I^{Tri}(t))$  or a stretched exponential decay ( $I^{Stretched}(t)$ ):

$$I^{Tri}(t) = A_1 e^{-t/\tau_1} + A_2 e^{-t/\tau_2} + A_3 e^{-t/\tau_3}$$
 [1]

$$I^{Tri}(t) = A_1 e^{-t/\tau_1} + A_2 e^{-t/\tau_2} + A_3 e^{-t/\tau_3}$$

$$I^{Stretched}(t) = \text{Aexp}\left(-\left(\frac{t}{\tau}\right)^{\gamma}\right)$$
[1]

where  $A_i$ ,  $\tau_i$ , and  $\gamma$  are treated as fitting parameters. Average lifetimes were calculated with the *amplitude average lifetime* (35):

$$\langle \tau \rangle_{Triexponential} = \frac{A_1 \tau_1 + A_2 \tau_2 + A_3 \tau_3}{A_1 + A_2 + A_3}$$

$$\langle \tau \rangle_{Stretched} = \frac{\tau}{\gamma} \Gamma \left( \frac{1}{\gamma} \right)$$
[4]

$$\langle \tau \rangle_{Stretched} = \frac{\tau}{\gamma} \Gamma \left( \frac{1}{\gamma} \right)$$
 [4]

where  $\Gamma$  is the gamma function.

# **Computational Methods:**

DFT: Density Functional Theory (DFT) calculations were performed with plane wave DFT in Vienna Ab initio Simulation Package (VASP) (36,37). All exchange-correlation functionals were described by the Perdew-Burke-Ernzerhof Generalized Gradient Approximation (PBE-GGA) (38), and the Projector Augmented Wave (PAW) (36,39,40) method approximated core electrons. The structure was relaxed until all forces and the self-consistent field energies were less than 0.01 eV/Å and 1E-5 eV, respectively. The Brillouin zone was sampled with a k-point density of 8 (Å<sup>-1</sup>)<sup>-1</sup> with an automatic Monkhorst-Pack grid (41). The kinetic energy cutoff was 550 eV. The structure contained at least 15 Å of vacuum spacing between adjacent sheets. Energies shown in Figure 5c are calculated as follows:

$$E = \frac{E_{Si_XH_XO_Y} - x * E_{SiH} - y * E_O}{y}$$
 [5]

where  $E_O = E_{H_2O} - E_{H_2}$ .

## Acknowledgments

This work was supported by the Department of Defense (DoD) Air Force Office of Scientific Research (AFOSR) Young Investigator Program (Grant # FA9550-17-1-0170) and the National Science Foundation CAREER Award (Grant # 1847370). Use of the Advanced Photon Source at Argonne National Laboratory was supported by the U. S. Department of Energy, Office of Science, Office of Basic Energy Sciences, under Contract No. DE-AC02-06CH11357. BJR acknowledges support from the National Science Foundation Graduate Research Fellowship Program under DGE 1744592. Any opinions, findings, and conclusions or recommendations expressed in this material are those of the authors and do not necessarily reflect the views of the National Science Foundation. BJR would like to thank Narayan Acharya for useful edits to the manuscript. Use of the Center for Nanoscale Materials, an Office of Science user facility, was supported by the U.S. Department of Energy, Office of Science, Office of Basic Energy Sciences, under Contract No. DE-AC02-06CH11357.

## References

- 1. S. Lukman, L. Ding, L. Xu, Y. Tao, A. C. Riis-Jensen, G. Zhang, Q. Y. S. Wu, M. Yang, S. Luo, C. Hsu, L. Yao, G. Liang, H. Lin, Y. W. Zhang, K. S. Thygesen, Q. J. Wang, Y. Feng, and J. Teng, *Nat. Nanotechnol.* **15**, 675–682 (2020).
- 2. X. Hu, B. Koiller, and S. Das Sarma, *Phys. Rev. B* **71**, (2005).
- 3. S. B. Desai, S. R. Madhvapathy, A. B. Sachid, J. P. Llinas, Q. Wang, G. H. Ahn, G. Pitner, M. J. Kim, J. Bokor, C. Hu, H.-S. P. Wong, and A. Javey, *Science* **354**, 99–102 (2016).
- 4. K. L. Low, W. Huang, Y. C. Yeo, and G. Liang, *IEEE Trans. Electron Devices* **61**, 1590–1598 (2014).
- 5. J. M. Caruge, J. E. Halpert, V. Wood, V. Bulović, and M. G. Bawendi, *Nat. Photonics* **2,** 247–250 (2008).
- 6. G. H. Carey, A. L. Abdelhady, Z. Ning, S. M. Thon, O. M. Bakr, and E. H. Sargent, *Chem. Rev.* **115**, 12732–12763 (2015).
- 7. Grätzel, M. Nat. Mater. 13, 838–842 (2014).
- 8. F. Maier-Flaig, J. Rinck, M. Stephan, T. Bocksrocker, M. Bruns, C. Kübel, A. K. Powell, G. A. Ozin, and U. Lemmer, *Nano Lett.* **13**, 475–480 (2013).

- 9. M. S. Ferris, A. P. Chesney, B. J. Ryan, U. Ramesh, M. G. Panthani, and K. J. Cash, *Sens. Actuators B Chem.* **331**, 129350 (2021).
- 10. F. Erogbogbo, K.-T. Yong, I. Roy, G. Xu, P. N. Prasad, and M. T. Swihart, *ACS Nano* **2**, 873–878 (2008).
- 11. C. A. Mirkin, and T. A. Taton, *Nature* **405**, 626–627 (2000).
- 12. K.-Y. Cheng, R. Anthony, U. R. Kortshagen, and R. J. Holmes, *Nano Lett.* **11,** 1952–1956 (2011).
- 13. M. Dasog, G. B. De los Reyes, L. V. Titova, F. A. Hegmann, and J. G. C. Veinot, *ACS Nano* **8**, 9636–9648 (2014).
- 14. G. T. Reed, A. P. Knights, *Prospects for Silicon Light-Emitting Devices*, p. 223-250, John Wiley & Sons, Ltd (2004).
- 15. F. Sangghaleh, I. Sychugov, Z. Yang, J. G. C. Veinot, and J. Linnros, *ACS Nano* 9, 7097–7104 (2015).
- 16. G. M. Carroll, R. Limpens, and N. R. Neale, Nano Lett. (2018).
- 17. W. D. A. M. de Boer, D. Timmerman, K. Dohnalová, I. N. Yassievich, H. Zhang, W. J. Buma, and T. Gregorkiewicz, *Nat. Nanotechnol.* **5**, 878–884 (2010).
- 18. X. Wen, P. Zhang, T. A. Smith, R. J. Anthony, U. R. Kortshagen, P. Yu, Y. Feng, S. Shrestha, G. Coniber, and S. Huang, *Sci. Rep.* **5**, 12469 (2015).
- 19. B. J. Ryan, M. P. Hanrahan, Y. Wang, U. Ramesh, C. K. A. Nyamekye, R. D. Nelson, Z. Liu, C. Huang, B. Whitehead, J. Wang, L. T. Roling, E. A. Smith, A. J. Rossini, and M. G. Panthani, *Chem. Mater.* **32**, 795–804 (2020).
- 20. S. W. Kim, J. Lee, J. H. Sung, D. J. Seo, I. Kim, M. H. Jo, B. W. Kwon, W. K. Choi, and H. J. Choi, *ACS Nano* **8**, 6556–6562 (2014).
- 21. H. Okamoto, Y. Kumai, Y. Sugiyama, T. Mitsuoka, K. Nakanishi, T. Ohta, H. Nozaki, S. Yamaguchi, S. Shirai, and H. Nakano, *J. Am. Chem. Soc.* **132**, 2710–2718 (2010).
- S. Z. Butler, S. M. Hollen, L. Cao, Y. Cui, J. A. Gupta, H. R. Gutiérrez, T. F. Heinz, S. Sae Hong, J. Huang, A. F. Ismach, E. Johnston-Halperin, M. Kuno, V. V. Plashnitsa, R. D. Robinson, R. S. Ruoff, S. Salahuddin, J. Shan, L. Shi, O. G. Michael Spencer, M. Terrones, W. Windl, and J. E. Goldberger, ACS Nano 7, 2898-2926 (2013).
- 23. H. Nakano, M. Ishii, and H. Nakamura, Chem. Commun. 2945–2947 (2005).
- 24. P. Kubelka, and F. Munk, *Z Techn Phys.* **12**, 593–601 (1931).
- 25. M. Sykora, L. Mangolini, R. D. Schaller, U. Kortshagen, D. Jurbergs, and V. I. Klimov, *Phys. Rev. Lett.* **100**, 067401 (2008).
- 26. W. Paul, and D. A. Anderson, *Sol. Energy Mater.* **5,** 229–316 (1981).
- 27. R. C. Chittick, J. H. Alexander, and H. F. Sterling, J. Electrochem. Soc. 116, 77 (1969).
- 28. H. Sai, T. Matsui, and K. Matsubara, Appl. Phys. Lett. 109, 183506 (2016).
- 29. J. Fan, and J. Kakalios, J. Appl. Phys. 74, 1799–1804 (1993).
- 30. Y. P. Varshni, *Physica* **34**, 149–154 (1967).
- 31. C. Delerue, G. Allan, C. Reynaud, O. Guillois, G. Ledoux, and F. Huisken, *Phys. Rev. B* **73**, 235318 (2006).
- 32. L. Pavesi, and M. Ceschini, *Phys. Rev. B* **48**, 17625–17628 (1993).
- 33. J. C. Phillips, J. Non-Cryst. Solids 357, 3853–3865 (2011).
- 34. B. H. Toby, and R. B. Von Dreele, *J. Appl. Crystallogr.* **46**, 544–549 (2013).
- 35. A. Sillen, and Y. Engelborghs, *Photochem. Photobiol.* 67, 475–486 (1998).
- 36. G. Kresse, and J. Furthmüller, *Phys. Rev. B* **54**, 11169–11186 (1996).
- 37. G. Kresse, and J. Furthmüller, *Comput. Mater. Sci.* **6**, 15–50 (1996).
- 38. J. P. Perdew, K. Burke, and M. Ernzerhof, *Phys. Rev. Lett.* **77**, 3865–3868 (1996).
- 39. G. Kresse, and D. Joubert, *Phys. Rev. B* **59**, 1758–1775 (1999).
- 40. P. E. Blöchl, *Phys. Rev. B* **50**, 17953–17979 (1994).

41. H. J. Monkhorst, and J. D. Pack, *Phys. Rev. B* 13, 5188–5192 (1976).